Hard x-ray telescopes to be onboard ASTRO-H

Hisamitsu Awaki,[1,*] Hideyo Kunieda,[2] Manabu Ishida,[3] Hironori Matsumoto,[2] Yasunori Babazaki,[2] Tadatsugu Demoto,[2] Akihiro Furuzawa,[2] Yoshito Haba,[4] Takayuki Hayashi,[3] Ryo Iizuka,[3] Kazunori Ishibashi,[2] Naoki Ishida,[5] Masayuki Itoh,[6] Toshihiro Iwase,[2] Tatsuro Kosaka,[7] Daichi Kurihara,[1] Yuuji Kuroda,[2] Yoshitomo Maeda,[3] Yoshifumi Meshino,[2] Ikuyuki Mitsuishi,[2] Yuusuke Miyata,[2] Takuya Miyazawa,[2] Hideyuki Mori,[2] Housei Nagano,[2] Yoshiharu Namba,[8] Yasushi Ogasaka,[9] Keiji Ogi,[1] Takashi Okajima,[10] Shigetaka Saji,[2] Fumiya Shimasaki,[2] Takuro Sato,[3,11] Toshiki Sato,[3,11] Satoshi Sugita,[1] Yoshio Suzuki,[12] Kenji Tachibana,[2] Sasagu Tachibana,[2] Shunya Takizawa,[2] Keisuke Tamura,[2] Yuzuru Tawara,[2] Tatsuharu Torii,[2] Kentato Uesugi,[12] Koujun Yamashita,[2] and Shigeo Yamauchi[13]

[1]Ehime University, Bunkyo-cho, Matsuyama, Ehime 790-8577, Japan

[2]Nagoya University, Furo-cho, Chikusa, Nagoya 464-8602, Japan

[3]ISAS/JAXA, Yoshinodai, Chuou, Sagamihara 229-8510, Japan

[4]Aichi University of Education, Igaya-cho, Kariya, Aichi 448-8542, Japan

[5]Tamagawa Engineering Co., Ltd., 1218-18, Chifuku, Kagiya, Kasugai, Aichi 480-0304, Japan

[6]Kobe University, Tsurukabuto, Nada, Kobe 657-8501, Japan

[7]Kochi University of Technology, Tosayamada-cho, Kami, Kochi 782-8502, Japan

[8]Chubu University, Matsumoto-cho, Kasugai, Aichi 487-8501, Japan

[9]Japan Science and Technology Agency, 5-1 Gobancho, Chiyoda, Tokyo 102-0076, Japan

[10]NASA's Goddard Space Flight Center, Greenbelt, Maryland 20771, USA

[11]Tokyo Metropolitan University, 1-1 Minami-Osawa, Hachioji, Tokyo 192-0397, Japan

[12]JASRI/SPring-8, Sayo-cho, Sayo, Hyogo 679-5198, Japan

[13]Nara Women's University, Kitauoyanishi-machi, Nara, Nara 630-8506, Japan

*Corresponding author: awaki@astro.phys.sci.ehime-u.ac.jp

Received 4 September 2014; revised 3 October 2014; accepted 5 October 2014; posted 8 October 2014 (Doc. ID 222374); published 4 November 2014

The new Japanese x-ray astronomy satellite, ASTRO-H, will carry two identical hard x-ray telescopes (HXTs), which cover the energy range of 5 to 80 keV. The HXT mirrors employ tightly nested, conically approximated thin-foil Wolter-I optics, and the mirror surfaces are coated with Pt/C depth-graded multilayers to enhance the hard x-ray effective area by means of Bragg reflection. The HXT comprises foils 120–450 mm in diameter and 200 mm in length, with a focal length of 12 m. To obtain a large effective area, 213 aluminum foils 0.2 mm in thickness are tightly nested confocally. The requirements for HXT are a total effective area of $>300\ \mathrm{cm}^2$ at 30 keV and an angular resolution of $<1.7'$ in half-power diameter (HPD). Fabrication of two HXTs has been completed, and the x-ray performance of each HXT was measured at a synchrotron radiation facility, SPring-8 BL20B2 in Japan. Angular resolutions

1559-128X/14/327664-13$15.00/0
© 2014 Optical Society of America

(HPD) of 1.9′ and 1.8′ at 30 keV were obtained for the full telescopes of HXT-1 and HXT-2, respectively. The total effective area of the two HXTs at 30 keV is 349 cm^2. © 2014 Optical Society of America
OCIS codes: (340.7470) X-ray mirrors; (350.1260) Astronomical optics.
http://dx.doi.org/10.1364/AO.53.007664

1. Introduction

X-ray telescopes onboard x-ray observatories have led to discoveries of high-energy phenomena in the Universe. The Einstein and ROSAT satellites revealed a number of x-ray point sources and diffuse x-ray emission in the soft x-ray band below ~4 keV [1]. The ASCA satellite [2] (launched in 1993) carried high-throughput x-ray telescopes with thin-substrate mirror shells for the first time, and the ASCA x-ray telescopes [3] made it possible to perform imaging spectroscopy with an energy range up to 10 keV, allowing one to examine the iron K emission line features (ca. 6–7 keV) with spatial information. The Chandra and XMM-Newton x-ray observatories launched in 1999 and 2000, respectively, enable us to observe objects with high spatial resolution (Chandra) and with large effective area (XMM-Newton). X-ray telescopes onboard Suzaku also cover the energy range below ~10 keV [4].

For hard x rays above 10 keV, the critical angle (θ_C) of total reflection quickly decreases with increasing x-ray energy E ($\theta_C \propto 1/E$). Thus, single-layer reflection mirrors used by previous missions have little effective area above ~10 keV. In order to increase reflectivity by means of Bragg reflection, the "multilayer supermirror" was introduced to replace the single-layer reflection mirror. A "supermirror" reflector consists of a thin substrate and a stack of depth-graded Pt/C multilayer coatings (with variable layer–pair thicknesses in the stack). In such a mirror design, soft x rays are reflected by the thicker Pt/C layer pairs close to the surface, while hard x-ray photons are reflected by thinner layer pairs close to the bottom. In turn, higher reflectivity at hard x-ray energies is achieved for a broad band.

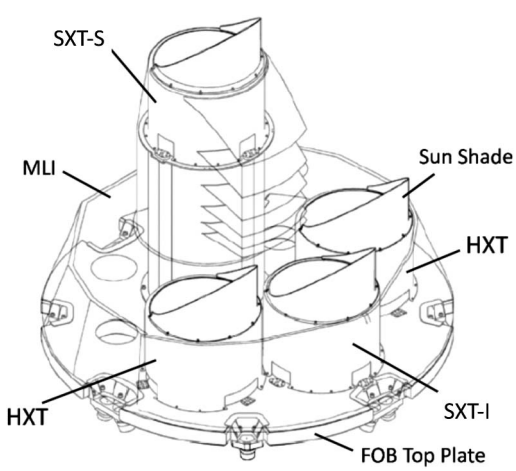

Fig. 1. Current configuration of the x-ray telescopes on the FOB top plate. The FOB top plate is covered with multilayer insulation (MLI). The MLI is transparent in this figure.

The first test mirror was produced in 1997 [5] as a Pt/C supermirror (26 layer pairs with changing thickness from 3 to 5 nm; the incident angle ~0.3° was chosen to enhance the reflectivity in the energy range of 24–36 keV). The first full hard x-ray telescope was launched as a US–Japan international balloon experiment—InFOCμS—in 2001 [6–8]. It consisted of a Pt/C multilayer supermirror and a CdZnTe detector. In its maiden and two later flights, several x-ray sources (including Cyg X-1) were imaged in 20–40 keV to demonstrate its performance. The success of the InFOCμS mission has been inherited by the Nuclear Spectroscopic Telescope Array (NuSTAR) mission [9], launched on 13 June 2012, and the ASTRO-H mission by JAXA.

The hard x-ray optic module onboard NuSTAR contains 133 nested multilayer-coated shells (Pt/C or W/Si) in a conical approximation to the Wolter-I optics. Each shell is composed of segmented mirrors formed by thermally slumping flat glass 0.2 mm thick. The angular resolution [half-power diameter (HPD)] has been measured to be 58″, where HPD is defined as the diameter of the circle centered on the peak of the x-ray image from a point-like source, in which the half of the entire x-ray flux is enclosed. The effective area at 30 keV is about 230 cm^2 [9].

ASTRO-H will be launched on HII-A, Japan's primary large-scale vehicle, in 2015 [10]. ASTRO-H will carry four x-ray telescopes (XRTs), two soft x-ray telescopes (SXTs), and two hard x-ray telescopes (HXTs) for the wide-band imaging spectroscopy between 0.3 and 80 keV. Two identical HXTs are mounted on the top plate of the fixed optical bench (FOB), while the hard x-ray imagers (HXIs), which are the focal plane detectors of the HXTs, are placed on the HXI plate of the extensible optical bench (EOB). A focal length of 12 m will be realized by extending the EOB. Figure 1 shows the current configuration of XRTs on the FOB top plate, including SXT for the x-ray CCD camera (SXT-I) and that for the x-ray microcalorimeter (SXT-S).

In the following section, we describe the design parameters of HXT, along with the designs of its precollimators (PCs) and thermal shields (TSs). In Section 2, the fabrication of HXT is described, and then the preliminary results of ground calibration of the integrated system are summarized in Section 4.

2. Design Parameters

A. Overview

The mission requirements for the ASTRO-H HXT are a total effective area of 300 cm^2 at 30 keV, and a HPD of 1.7′ at 30 keV [10]. ASTRO-H HXT will have a larger effective area than NuSTAR, while the angular resolution of the HXT will not be better. To meet the requirement for effective area, the ASTRO-H HXT mirrors employ tightly nested, conically approximated thin-foil Wolter-I optics, and the mirror surfaces are coated with Pt/C depth-graded multilayers similar to those of the InFOCμS telescopes. The basic design parameters of the proposed ASTRO-H HXT are as follows: 12 m focal length, 45 cm diameter telescope consisting of 20 cm long foils in two (primary and secondary) stages (see Table 1). The diameters of the innermost and the outermost reflectors are 120 and 450 mm, respectively.

The image blurring of thin-foil Wolter-I optics is caused by the figure errors of individual reflectors, uncertainties of positions of individual reflectors, the image asymmetry caused by an error of the alignment bar position, and a conical approximation of the Wolter-I optics [11]. To achieve the requirement for the HPD, we assigned the error budget on the HXT HPD as listed in Table 2 from the experience of the balloon-borne experiment.

B. Telescope Housing Design

Detailed design of HXT has been carried out based on the InFOCμS and SUMIT balloon-borne experiments [11], under the constraint of the space within the nose fairing of the HII-A rocket. Figure 2 shows a schematic view of the design of HXT. The diameter and height of the HXT housing are 480 and 509.4 mm, respectively. HXT has three mount tabs to be mounted on the FOB top plate, and consists of four components: two TSs, a PC, an x-ray mirror, and a reference cube.

Table 1. Design Parameters of ASTRO-H Hard X-Ray Telescope

Items	HXT
Focal length	12 m
Number of modules	2
Substrate	
Material	Aluminum
Substrate thickness	200 μm
Axial length	200 mm
Reflectors	
Material	Pt/C multilayer
Adhesive material	Epoxy
Adhesive thickness	20 μm
Number of nesting shells	213
Diameter of innermost reflector	120 mm
Diameter of outermost reflector	450 mm
Incident angle	0.07°–0.27°
Number of reflectors/telescope	1278
Geometrical area/telescope	968 cm^2
Weight/telescope	~62 kg

Table 2. Error Budget on the HXT HPD

Reflector figure error	1.4′
Positional error of reflector	0.7′
Bar positional error	0.4′
Conical approximation error	0.3′

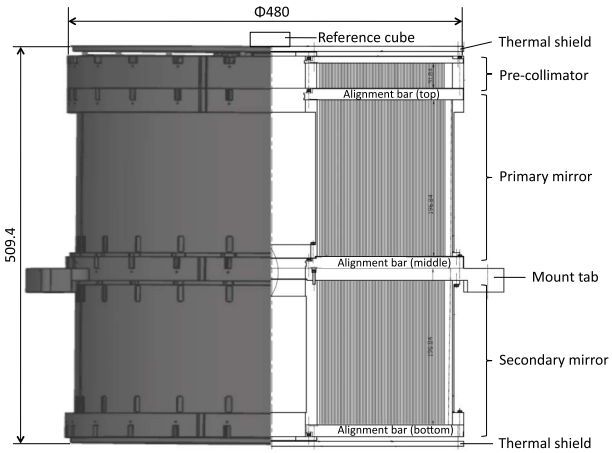

Fig. 2. Schematic view of the ASTRO-H HXT. The right part displays a cross section of HXT.

The ASTRO-H HXT mirrors are installed into a telescope housing, and are positioned by alignment bars as shown in Fig. 2. Each alignment bar has a series of grooves to hold the mirror reflectors. While the x-ray mirror housing of the Suzaku XRT is separated into primary and secondary parts, both parts of the mirror housing are unified in the ASTRO-H HXT. As a result, the bottom edge of the primary reflectors and the top edge of the secondary reflectors are held at their desired locations by the same alignment bars. Thanks to the unification, we can avoid misalignment between the primary and secondary reflectors. The alignment error is expected to be a few micrometers, which is determined by both manufacturing error and the groove width of the alignment bars.

The temperature of the HXT housing and mirror reflectors will be controlled at 22 ± 2°C during observations using a heater power control system. The temperature of 22°C is the room temperature of the clean room at Nagoya University, where the HXT was fabricated. To provide temperature stability of the HXT and to reduce temperature control heater power in orbit, the HXT housing is designed to be thermally isolated. We use a thermal insulator made of titanium alloy to reduce the thermal conductivity between the HXT housing and the top plate of FOB, and both the top and bottom apertures of the telescope are covered with TSs. Furthermore, to make the temperature of each mirror reflector uniform, the inner surface of the housing is black anodized. Details of the thermal design of HXT are described by Ito *et al.* [12].

After measuring the relative orientation of the HXT optical axis and the reference cube in a ground

calibration, the cube is used to reference the optical axis of the telescope.

C. Reflectors

The HXT mirror employs conically approximated thin-foil Wolter-I optics. The incident grazing angles of the reflectors range from 0.07° to 0.27°. To achieve high aperture efficiency despite the small incident angle, thinner substrates with longer length are preferred. Thus, we use a 0.2 mm aluminum substrate with 200 mm length. Based on the mirror inner and outer diameters, the focal length, the reflector height, and the reflector thickness, each reflector top and bottom radius can be derived such that on-axis x rays focus onto the focal plane without being blocked by adjacent reflectors. In other words, the nested reflector geometry is optimized to achieve the maximum on-axis effective area. Consequently, the 213 reflector shells are confocally nested.

The incident grazing angle at the outermost radius is 0.27°, which corresponds to the critical grazing angle of platinum for total reflection of a 18 keV photon. To enhance the reflectivity in hard x rays with $E > 20$ keV, we employ Bragg reflection. For Bragg reflection, reflectivity is enhanced when the Bragg condition is satisfied: $n\lambda = 2d\,\sin(\theta)$, where n is the order of reflection, λ is the wavelength of the incident x ray, d is the periodic length of the multilayers, and θ is the grazing angle of incidence. A simple multilayer (with constant d) shows a narrow energy/angular response. For astronomical applications, the narrow response is broadened by stacking multilayers with different sets of periodic length and numbers of layer pairs in the depth direction, which produces the "supermirror." A supermirror is designed so that the periodic length decreases from the top surface to the base substrate. X rays with higher energy, which have a longer penetration depth, are reflected by a deeper layer (see Fig. 3).

Because the reflectivity response strongly depends on the incident angle, we divided the reflectors into groups by the grazing incident angle, and then optimized the multilayer design for each reflector group. Table 3 describes the grouping definition. Although the original definition used Group ID from 1 to 9 [13], we have divided Group ID 1 into Group ID 901–904 and 1 in order to obtain a larger effective area [14]. Figure 4 demonstrates the x-ray reflectivity of three groups. The reflectivity curves are calculated with Sasaki's tables [15,16]. Groups 901 through 7 are designed to show a flat curve up to 78 keV, which corresponds to the Pt-K edge energy. The reflectivity of groups 8–10 falls at an energy lower than 70 keV because we designed the multilayer parameters for these groups with the limit of minimum d spacing of 2.4 nm, corresponding to the manufacturing limit on roughness.

The on-axis effective area of the designed mirror at an energy E can be calculated by $S_{\mathrm{eff,design}}(E) = \sum_i S_i R_i(E,\theta_i)^2$, where S_i is the projected area of the reflector (shell number i) and $R_i(E,\theta_i)$ is the reflectivity at the incident angle θ_i to the reflector at the given energy. In order to derive S_i, the obscuration by the housing structures, such as alignment bars, and segment boundaries, is also taken into account. The aperture efficiency, the usable projected area for x-ray focusing over the open aperture area, is 0.67. The x-ray reflectivity $R_i(E,\theta_i)$ is calculated with the designed multilayer parameters and a given interfacial roughness.

In the real HXT, the mirror effective area may be reduced from the design value due to imperfection in the figure and positioning uncertainty of the reflectors, which cause x-ray reflections off the normal

Table 3. Grouping Definition for Optimizing Multilayer Parameters

Group ID	Incident Angles (°)	Foil ID
901	0.072–0.079	1–11
902	0.08–0.089	12–24
903	0.09–0.099	25–38
904	0.10–0.109	39–53
1	0.11–0.116	54–68
2	0.117–0.128	69–84
3	0.129–0.144	85–103
4	0.145–0.159	104–119
5	0.160–0.178	120–138
6	0.179–0.196	139–155
7	0.197–0.218	156–174
8	0.219–0.241	175–193
9	0.242–0.266	194–212
10	0.268	213

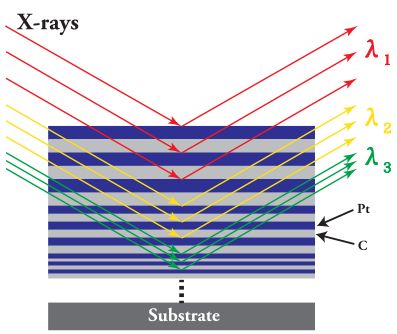

Fig. 3. Schematic view of Bragg reflection in depth-graded multilayer. $\lambda_{1,2,3}$ indicate the wavelength of x rays, $\lambda_1 > \lambda_2 > \lambda_3$. The x rays with shorter wavelength λ_3 are reflected by a deeper layer.

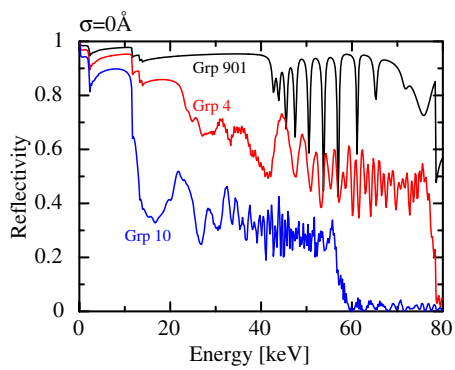

Fig. 4. Reflectivity curves of groups 901, 4, and 10. Definition of the group is described in Table 3.

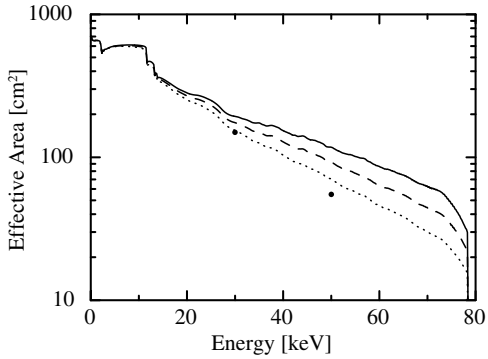

Fig. 5. On-axis effective area of HXT (one telescope) with interfacial roughness of 0.3 nm (solid line), 0.4 nm (dashed line), and 0.5 nm (dotted line). Assumed throughput is 0.75. Filled circles show the requirements.

x-ray path. Thus x rays may be blocked by adjacent reflectors or the housing structure, resulting in a loss of effective area. This reduction factor f_{TP}, which is called throughput (TP), needs to be taken into account. The TP can be easily incorporated into the effective area equation assuming that it is energy-independent, and the actual effective area can be estimated by $S_{\mathrm{eff,actual}} = f_{\mathrm{TP}} S_{\mathrm{eff,design}}$. Figure 5 shows the expected effective area assuming interfacial roughness of 0.3, 0.4, and 0.5 nm (Debye–Waller factor). A throughput of 0.75 is adopted and is based on the measured results of the hard x-ray mirror for the SUMIT experiment [11]. Filled circles show requirements for the effective area of HXT (150 cm^2 at 30 keV, 55 cm^2 at 50 keV for a single telescope).

The mirror vignetting function, the effective area as a function of the off-axis angle divided by the on-axis effective area, is calculated by a ray-tracing simulator. The vignetting functions at energies of 10, 30, and 50 keV are shown in Fig. 6 for the ideal case (the reflector figure error and alignment error are not included). The mirror field of view (FOV) can be defined by the FWHM of the vignetting function. The FOVs are estimated to be 8.2′, 6.4′, and 5.3′ at 10, 30, and 50 keV, respectively.

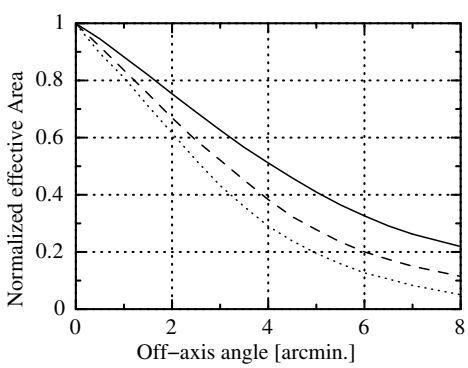

Fig. 6. Vignetting functions at $E = 10$ keV (solid line), 30 keV (dashed line), and 50 keV (dotted line) calculated by the ray-tracing simulator for the ideal reflector case. An interfacial roughness of 0.3 nm is assumed.

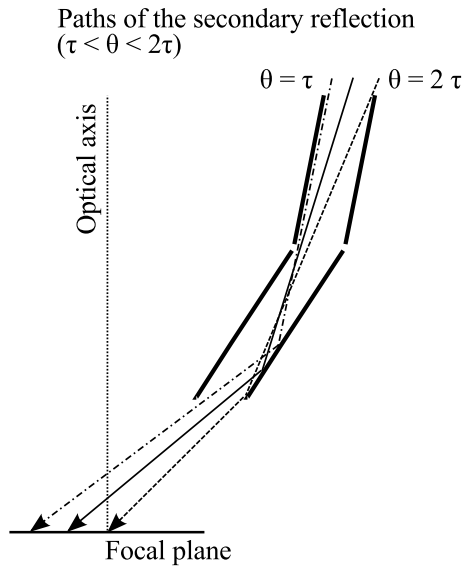

Fig. 7. Schematic view of paths of the secondary reflection. The secondary reflection is caused only by secondary foils with $\tau < \theta < 2\tau$, where τ represents a tilting angle of the corresponding primary foil, and θ is the incident angle of x rays.

D. Precollimator Design

Some off-axis x rays reach the focal plane without the normal double reflection. These x rays create a ghost image in the detector FOV, called stray light. The most intensive stray light contaminating the detector is due to off-axis x rays that pass through just above the edge of the primary foils and are reflected once on the secondary foils (referred to as secondary reflection) [17] (see Fig. 7). The stray light may be caused by a bright point source located outside of the telescope FOV or a diffuse source extended over the telescope FOV, such as a cluster of galaxies or the cosmic x-ray background. The ghost image of stray light acts as a diffuse background, which degrades the detection limit.

In order to reduce stray light, some XRT systems are equipped with a baffle structure (PC) in front of the mirrors. The baffle consists of thin cylindrical shells, which are called blades. The reduction rate of the stray light depends on the height, thickness, and material of the blades [18,19]. There is a trade-off between stray-light reduction and the telescope FOV, since the PC mount makes the telescope vignetting narrower. Thus, we need to optimize the blade properties.

The current design parameters of the HXT PC are summarized in Table 4. The blade thickness and

Table 4. Design Parameters of the HXT Precollimator Blades

Items	Parameters
Thickness	150 μm
Height	50 mm
Length	35 mm
Material	Aluminum alloy

height (measured from the top edge of the primary foils) are 150 μm and 50 mm, respectively. The blades are thinner than the mirror foils. This blade height is adequate to eliminate the secondary reflection from a >20′ off-axis source. The blade is required to be taller for reducing the stray light at a smaller incident angle, since the blade height is proportional to $1/\tan\theta$ (see right panel of Fig. 5 in Mori *et al.* [17]). However, the HXT FOV is found to shrink rapidly as the blade height is larger than 50 mm [19]. Thus, we have decided to make the heights of all blades 50 mm.

Aluminum is selected as the blade material, because we have experience in producing PC blades made of aluminum for the Suzaku XRTs. We note that the aluminum becomes transparent above 50 keV and then the stray light penetrating the blades emerges at >20′ off-axis. However, the flux level of the stray light is smaller than the flux level of the cosmic x-ray background ($<4\times10^{-4}$) [19].

In the ASTRO-H HXT, the PC is integrated into the mirror housing in order to reduce stray light efficiently without any loss of the on-axis effective area due to misalignment between the PC blades and the mirror foils (see Fig. 2).

E. Thermal Shield Design

The main purpose of the TS, together with the heater attached to the HXT housing, is to keep the HXT mirror temperature within a specified range as described above [20]. The TSs are made of a polyethylene terephthalate (PET) film, coated with an aluminum layer with a thickness of 30 nm. The thermo-optical properties (solar absorptivity and thermal emissivity) of the aluminum layer side were measured to be 0.107 and 0.034, respectively. This TS also works to block optical light from the sky and from the surface of the Earth illuminated by the Sun. We use a PET film as thin as 2.5 μm for two TSs set on both the top and bottom of the HXT. The x-ray transmission of 5 μm (2 μm × 2.5 μm) PET is 98% at an energy of 5 keV, which is the lower end of the energy band of the HXI. In order to provide enough mechanical strength to enable the TS to survive in various environments, a stainless steel mesh with a wire pitch, width, and thickness of 3, 0.1, and 0.25 mm, respectively, is used to support the thin film (Fig. 8). Since soft x rays are blocked by the stainless steel mesh, the transmission of soft x rays down to 8 keV is ~93% (see Fig. 9).

Fig. 8. Stainless steel mesh of the TS for supporting the thin film.

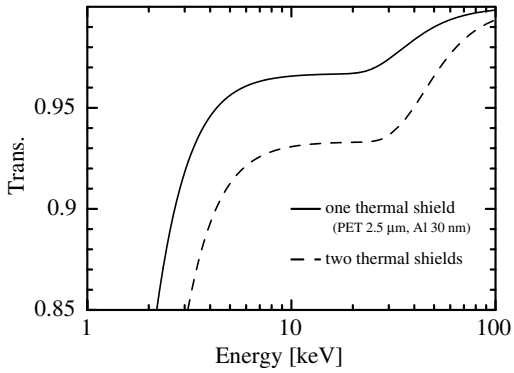

Fig. 9. X-ray transmission of the HXT TS. The transmission is calculated with the photoabsorption table by Henke *et al.* [21]. The solid line is for one TS, PET 2.5 μm with Al 30 nm, and the dashed line is for two TSs.

F. Reference Cube

The HXT vignetting curve is very sharp, especially at higher energies as shown in Fig. 6. Thus the effective area is reduced to 80% at $E = 50$ keV with only 1′ offset from the optical axis. This means that if the optical axes of two HXTs are misaligned, the total effective area of HXT-1 and HXT-2 is reduced due to the vignetting. We thus aim to establish a method to measure the orientation of HXT with an accuracy of ~5″, and to adjust the orientations of two HXTs.

In order to find the telescope optical axis, we equip each HXT with a reference cube mirror. The reference cube mirror is 15 mm on a side, and the accuracy of the orientation of each face of the cube mirror is within 5″. The reference cube is glued to a cube base, which is fixed at the center of the telescope. By calibrating the orientation of the reference cube relative to the HXT optical axis, we can find the optical axis by measurements of the cube orientation.

The spacecraft also has the so-called "satellite reference cube mirror" attached at the base plate, which represents the orientation of the spacecraft with a measurement accuracy of ~1″. By using the reference cube mounted on each telescope and the satellite reference cube, we can align the optical axis of each telescope to the satellite Z axis. For the alignment of the HXT orientation, we plan to insert mechanical shims beneath the mount tabs of the HXT. Using the shims in a unit of 10 μm thickness, we can adjust the orientation in units of ~5″.

3. Fabrication of HXT

A. Mirror Foil Fabrication

The reflectors are realized by the epoxy-replication method, in which a depth-graded Pt/C multilayer is sputtered onto the smooth surface of a glass tube and transferred to a conically shaped aluminum substrate with epoxy glue [22]. The basic technology for fabricating the ASTRO-H HXT has been established

through the balloon-borne experiments, "InFOCμS" and "SUMIT."

The aluminum foils were cut into a fan shape and stacked onto a shaping mandrel. The foils were pressed onto the shaping mandrel with air pressure and formed into a precise conical shape at 200 °C for 12 h in an oven. The shaping mandrel had a small figure error that was less than 6 μm peak-to-bottom, and the shaped substrate had the same error. Cone angles of the substrates ranged from 0.07° to 0.27° for primary reflectors and from 0.21° to 0.81° for secondary ones.

The depth-graded multilayer was deposited onto a cylindrical glass mandrel using a DC-magnetron sputtering system. The surface of the glass mandrel had a quite small microroughness of a few tenths of a nanometer, and the large-scale figure error was less than 7 μm peak-to-bottom over a 200 mm length. After the deposition, epoxy was sprayed on the inner side of the substrate with a 20 μm thickness, which is thick enough to fill the figure error between the glass mandrel and the substrate. After spraying epoxy, the substrate was glued onto the multilayer-coated mandrel, and the epoxy was cured at 50 °C for 14 h in an oven. When the epoxy layer was cured, it was separated at the boundary between the multilayer and the glass mandrel. We removed excess glue by shaving the edge of the substrate, thus completing a reflector for the HXT.

We produced more than 4000 mirror reflectors over about three years [23]. Each reflector was measured with optical light, and 1278 mirror reflectors with a high imaging quality were selected for each telescope. The average half-power width of the selected reflectors is about 0.8′. We also performed a random sampling inspection, in which the x-ray reflectivity of a sample reflector was measured at the energy of 8.0 keV in order to evaluate the quality of the mirror reflectors. The average surface roughness of mirror reflectors passing the inspection is 0.4 nm.

B. Overview of BL20B2 at SPring-8

During the assembly of HXT, we tuned the position of the alignment bars by using the x-ray beam at the SPring-8 beam line BL20B2. SPring-8 is a third-generation synchrotron radiation facility located in Hyogo, Japan. The acceleration energy of an electron beam is 8 GeV. The fluctuation of the ring current is on the order of 10^{-3}, which is well below our requirement. The beam line BL20B2 is a bending-magnet beam line in the Biomedical Imaging Center, allocated to medical applications and various imaging techniques in the energy range of 5–113 keV [24]. The total length of this beam line is 215 m from the front end. The BL20B2 consists of an optics hutch and three experimental hutches. The three experimental hutches are located 44, 203, and 211 m from the light source, referred to as hutches 1, 2, and 3, respectively. By using hutches 2 and 3, a 16 m long experimental hutch is available for calibrations of HXTs that have a long focal length.

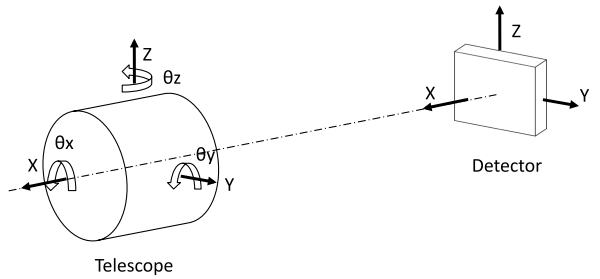

Fig. 10. Definition of the coordinates of the HXT measurement system at SPring-8.

The x-ray beam, which is extracted from the bending magnet with a horizontal acceptance angle of 1.5 mrad, spreads to a 300 mm wide beam at hutch 2; therefore, the available maximum x-ray beam size is 300 mm (horizontal) × 20 mm (vertical). The divergence angle of the x-ray beam at 200 m is ~1″ per mm. The Si double crystal monochromator (DCM) is located in the optics hutch 36.8 m from the light source, and the continuum x rays are monochromatized by the DCM. By changing crystal planes of 111 (5.0 to 37.5 keV), 311 (8.4 to 72.5 keV), and 511 (13.5 to 113.3 keV), a wide energy range is available from 5 to 113 keV. The energy resolution ($\Delta E/E$) of the available x-ray beam achieves $<10^{-4}$ in this energy region. This is well within our requirement for monochromaticity. Calculated photon flux densities at hutches 1 and 3 are about 6×10^7 photons s^{-1} mA^{-1} mm^{-1} and 1.5×10^7 photons s^{-1} mA^{-1} mm^{-1}, respectively, at 30 keV with Si 311 reflections. It warrants mention that synchrotron radiation is far brighter than a conventional x-ray source.

For x-ray measurements of HXT at SPring-8 BL20B2, an HXT and an x-ray detector were set on motorized positioning stages in hutches 2 and 3, respectively. The positioning stages in hutch 2 allow three-axis rotations (θ_X, θ_Y, and θ_Z) and two-axis translations (Y and Z), while those in hutch 3 allow three-axis translation (X, Y, and Z). Figure 10 indicates the definition of the coordinate of the measurement system. The measurement systems at SPring-8 BL20B2 are described in more detail by Ogasaka *et al.* (2008) [25] and Miyazawa *et al.* (2008, 2010) [26,27].

C. Assembly and Alignment Process

Production of the housing and alignment bars for HXT-1 was completed in 2011, and that for HXT-2 was completed in 2012. An alignment bar has a series of 213 grooves to hold mirror reflectors. High-precision processing is required to fabricate the alignment bars in order to position reflector foils accurately. We cut the grooves with a wire electric discharge machine, and confirmed that the grooves were accurately processed with an error of <10 μm by using a laser profiler, NH-6 (MITAKA Kohki Co. Ltd.). The image blurring due to the position error of the groove is estimated to be ~20″.

At first, we integrated the secondary mirror housing, and then installed the secondary 639 mirrors into the secondary housing. When the reflectors are installed into the mirror housing, the radial positions of the alignment bars are adjusted with an accuracy of 0.1 mm, using the marked lines cut on the bars. However, in order to achieve an image quality of <2′, we need a fine tuning of the radial positions with a resolution of 1 μm. To adjust the bar positions to this accuracy, we used piezo linear actuators (Piezo LEGS Linear Twin 20N) manufactured by PiezoMotor. A body of a piezo linear actuator was fixed on the telescope housing, and the rod of the piezo actuator was connected to the alignment bar. The XRT with 24 attached piezo actuators is shown in Fig. 11.

Each alignment bar was fastened to the telescope housing by two screws. Loosening the screws, the bar could move in the radial direction within a clearance of the screw holes, ±0.2 mm. There is a triangle-shaped marker on each side of an alignment bar (see Fig. 12). A 5 mm × 5 mm square x-ray beam illuminating the triangle-shaped marker provides a silhouette of the triangle-shaped markers in an x-ray image. Figure 12 shows the silhouettes of the triangle-shaped markers of the bottom, middle, and top bars. In installing only secondary mirrors, the silhouettes of the top bars are absent due to the lack of top bars. Measuring the position of the triangle-shaped markers in the x-ray image, we have adjusted the middle bar positions within a displacement of ±11 μm, which is nearly equal to the pixel scale of the x-ray detector (scintillator + CCD).

For the tuning of the bottom bars, we set x-ray detectors at the focal length of the secondary reflector, and then obtained a local spot image at the focal plane of the secondary reflectors when illuminated by an x-ray beam. If a bar position is misaligned, the center position of the local spot image is shifted from the focal position of the secondary reflectors. We tuned the position of each bar by shifting the center position by <0.5′.

Next, we assembled the primary mirror housing on the secondary mirror housing, and then installed the primary 639 mirrors. Fine tuning of the alignment

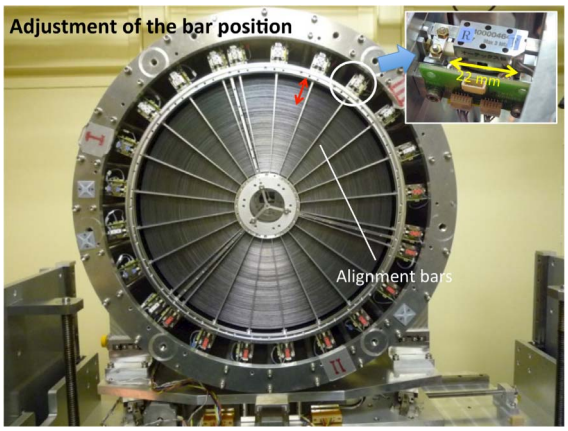

Fig. 11. XRT with piezo actuators.

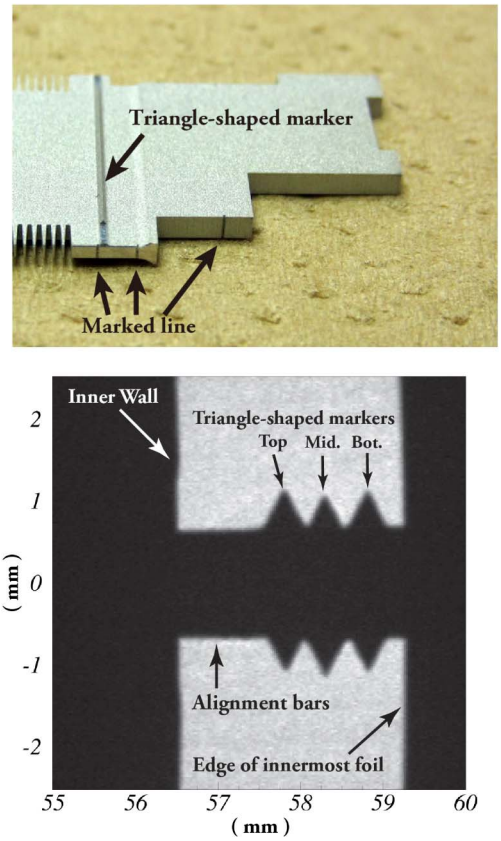

Fig. 12. Triangle-shaped marker on an alignment bar (upper panel) and silhouette of the triangle-shaped markers of alignment bars in an x-ray image (lower panel). There is a triangle-shaped marker on the opposite side of the bar. The positions of the marker are different for the top, middle, and bottom bars, so that we can see all markers in the silhouette.

bars for accurate positioning of the primary mirrors was also performed at SPring-8. The telescope was illuminated with an x-ray beam collimated to 20(H) × 10(V) mm^2, and a local spot image at the focal plane was obtained. In a similar manner to the adjustment of the bottom bars, we corrected the discrepancy of the local spot image. After tuning, the focal plane image became a round shape with a standard deviation of the local image shift of ~0.1′. Figure 13 demonstrates a result of the tuning. The standard deviation corresponds to the HPD of

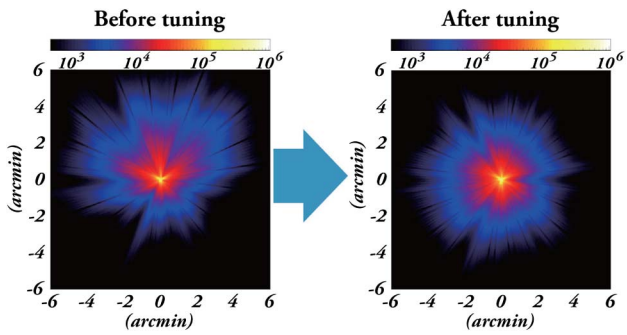

Fig. 13. X-ray images before tuning (left) and after tuning (right). After tuning, the x-ray image had a round shape.

Fig. 14. HXT-1 mirror component.

0.14′. Since the HPD of HXT is expected to be 0.7′, an image blurring due to misalignment of the alignment bars is negligible. After tuning, we fixed the alignment bars on the housing by screws and glues.

Figure 14 shows the HXT-1 mirror component after integration of primary and secondary mirrors. The mirror part of HXT-1 was completed in May 2012. One year later, HXT-2 was also completed.

D. Integration of Precollimator

PC blades were produced at ISAS/JAXA. The manufacturing process for the PC blade is similar to that for the mirror substrates described in Section 3.A [19]. We mounted a PC housing on the mirror component of HXT, and then installed the PC blades in the PC housing. Both the top and bottom of the PC blades are designed to be held by alignment bars. The alignment bars for the bottom of the PC blades had already been tuned, since the alignment bars are the same as those for the top of the primary mirrors as shown in Fig. 2. Thus, we adjusted the bar positions holding the top of the PC blades so as not to reduce the on-axis effective area of the telescope. After tuning, the reduction rates of the effective area due to the integration of the PC were found to be less than a few percent in the x-ray calibration at SPring-8.

We also measured the stray light at $E = 30$ keV in order to examine the effectiveness of the PC. The telescope was tilted at 12′ or 20′ from on-axis, and the detector was set at an offset position from the beam axis in order to detect the stray light. Figure 15 shows stray-light images at 12′ off-axis angle without and with the PC, and at 20′ off-axis angle with the PC. The main component of the stray light in these images is the secondary reflection described in Fig. 7. The rectangle in each image indicates the FOV of HXI. We compared the fluxes of stray lights with and without PC images, and we found that the stray light was reduced to 40% with the PC in the case of a 12′ off-axis angle. We also confirmed that almost all of the stray light could be reduced in the FOV of HXI at a 20′ off-axis angle with the PC.

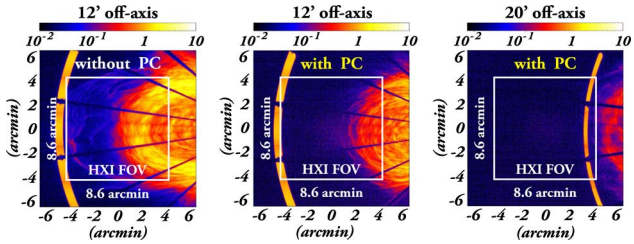

Fig. 15. Stray-light images at 12′ off-axis angle without and with PC (left and middle), and at 20′ off-axis angle with PC (right). The rectangle in each image indicates the FOV of the focal plane imager HXI. The circular arc in each image is caused by the direct x-ray beam passing through the clearance between the innermost reflector and the wall of the HXT housing.

4. Ground Calibration

A. X-Ray Measurement of HXT

X-ray light with small divergence is necessary for measuring both the effective area and the point spread function of HXT. We made an x-ray beam collimated into a rectangular shape 10 mm × 10 mm with a four-axis slit in front of the telescope. The collimated beam has a divergence of 10″, which is quite small in comparison with the HXT HPD. We adopted a mosaic exposure method by moving the two-axis translation stages in hutch 2 so that the aperture of one segment of the HXT was fully covered with the collimated x-ray beams. Figure 16 displays an example of a mosaic exposure map covering the full aperture of one segment. In the mosaic exposure method, the stages in hutch 3 moved synchronously with the stages in hutch 2. By changing telescope segments through rotating the telescope in the θ_X direction, the full aperture of one telescope was illuminated by the x-ray beams.

The calibration items at SPring-8 are listed in Table 5. We had a plan to measure the x-ray performance of the HXT by the mosaic method at 20, 30, 40,

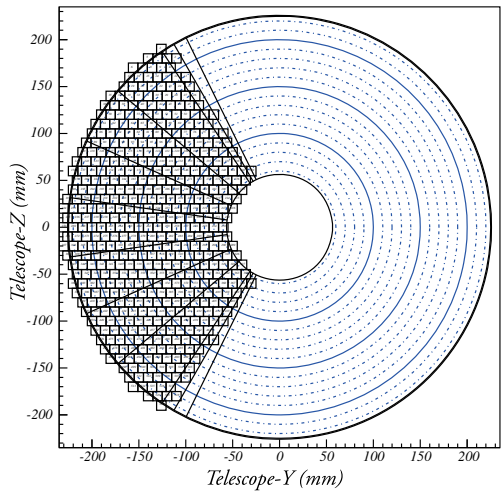

Fig. 16. Example of a mosaic exposure map covering the full aperture of one segment. Small squares present the size of the collimated x-ray beam, 10 mm × 10 mm square.

Table 5. Calibration Items of HXTs at SPring-8[a]

Energy (keV)	20	30	40	50	60	70
PSF/EEF +effective area	2	1,2	1,2	1,2	1,2	1,2
Vignetting function		1		1,2		
Stray light		1,2			2	

[a]1: HXT-1, 2: HXT-2.

50, 60, and 70 keV, but we did not have time to measure the x-ray performance of HXT-1 at 20 keV. We also measured detailed energy dependence of the effective area of HXT-2 in the energy range from 20 to 70 keV with $\Delta E = 1$ keV in order to find a fine structure of the effective area due to Bragg reflection. In this paper, we describe only preliminary results of basic items, such as the HPD, effective area, and vignetting function. Figure 17 shows an on-axis x-ray image with a size of 12′ square at 30 keV. The focal plane detector was an image intensifier (C7776) coupled to a CCD image sensor (C4480) made by HAMAMATSU Photonics K. K. The plate scale and the number of effective pixels are 19.3 μm/pixel and 4000(H) × 2624(V), respectively. Since the x-ray detection sensitivity of the focal plane detector was not uniform, we performed a simple flat field correction.

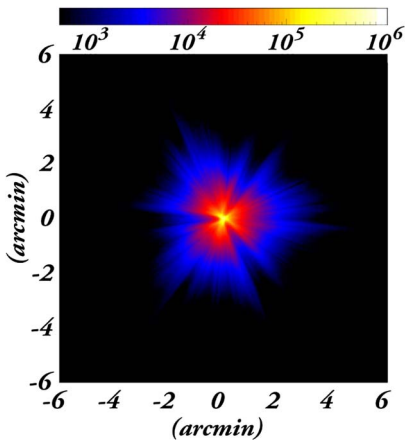

Fig. 17. On-axis image of HXT-1 at 30 keV. The image is a square 12′ on a side.

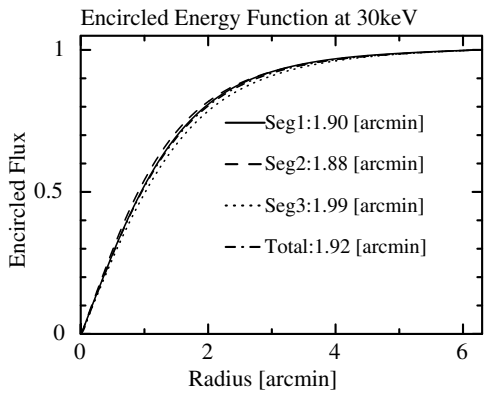

Fig. 18. Encircled energy function of HXT-1 at 30 keV. The encircled flux is normalized at a radius of 6′.

Table 6. Preliminary Result on X-Ray Performance of HXTs[a]

Energy (keV)	Half-Power Diameter (′)	Effective Area (cm^2)
	HXT-1 HXT-2	HXT-1 HXT-2
20	—, 1.90	—, 288
30	1.92, 1.88	170, 178
40	1.94, 1.88	123, 125
50	1.80, 1.78	82, 82
60	1.67, 1.67	50, 49
70	1.49, 1.55	24.5, 24.8

[a]Typical error: 0.1′ in HPD, about 2% in effective area.

The flat field has some ambiguity due to both the complex characteristics of the detector and a drift of the x-ray flux. Thus the results may contain a systematic error of about 10%.

We deduced the encircled energy function of each segment and a sum of the segments 1, 2, and 3, normalized at a radius of 6′ (Fig. 18), and estimated the HPDs of HXTs as listed in Table 6. The HPDs of HXT-1 and HXT-2 at 30 keV were estimated to be 1.92′ and 1.88′, respectively. The main sources of the HPD are considered to be both figure errors and positional errors of reflectors, since the HPD can be explained by a superposition of the HPWs of spot images. The HPD of the ASTRO-H HXT depends on the incident x-ray energy; in contrast, that of the Suzaku XRT does not significantly depend on the energy of the incident x rays below 10 keV. This dependency in the HXT is because high-energy photons have high reflectivity over a smaller grazing angle range and because the waviness of the mirror reflectors at the inner radius is smaller than that at the outer radius. We note that the image quality is a function of the surface roughness of reflectors (e.g., Spiga (2007) [28]). Although a power spectral density of the HXT reflector was not available, we estimated an HPD caused by x-ray scattering to be about 0.5′ at 50 keV at an incident angle of 0.15° and $\sigma = 0.4$ nm from Fig. 4 and Eq. (43) in Spiga (2007) [28]. The image blurring by the x-ray scattering would not be a main source of the HXT HPD.

The effective areas of HXT-1 and HXT-2 were deduced to be about 170 and 178 cm^2, respectively, at 30 keV, by accumulating the photons within a radius of 4.3′. The measured values are plotted on the effective area estimated from the HXT design (see Fig. 19) [13]. We found that the measured values are roughly equal to the estimation in the case of $\sigma = 0.41$ nm and $f_{\mathrm{TP}} = 0.75$. The roughness is consistent with the result of the roughness described in Section 3.A.

Table 6 shows a summary of the HPD and effective area. The x-ray performance of HXT-1 and HXT-2 is close to the requirement for HXT.

B. Vignetting

We measured the dependence of the effective area on an off-axis angle by rotating the θ_Y or θ_Z stage shown in Fig. 10. The off-axis angle ranges from −7′ to +7′ with a pitch of 1′ in the θ_Y direction, and from −4′ to +4′ with a pitch of 0.5′ in the θ_Z direction. In order to

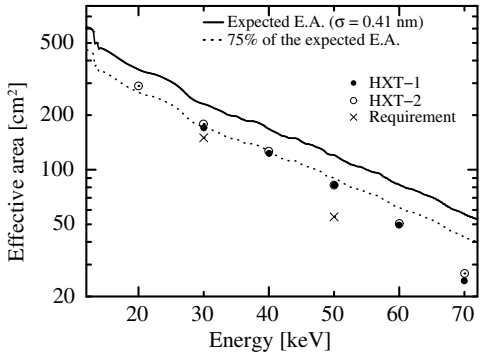

Fig. 19. Effective area of HXT. Filled and open circles show effective areas of HXT-1 and HXT-2 deduced from the measurements at SPring-8, respectively. Crosses show the requirement to HXT. Solid line shows estimation of the effective area in $\sigma = 0.41$ nm and $f_{\mathrm{TP}} = 1$. The dotted line is in $f_{\mathrm{TP}} = 0.75$.

save the measurement time for obtaining the effective area at one off-axis angle, one segment of HXT was sparsely covered with 10 mm × 10 mm x-ray beams. The coverage is about 25%. We confirmed that the effective area with a sparse mosaic coverage did not differ significantly from that with a full mosaic coverage. The measurements were performed at energies of 30 and 50 keV for HXT-1, and at an energy of 50 keV for HXT-2. We made a vignetting curve by calculating the number of photons collected within a radius of 4.3′ of an x-ray image in each off-axis angle. Figure 20 plots the number of collected photons as a function of the off-axis angle (vignetting curve), which is normalized at the off-axis angle = 0. We fitted the vignetting curves with a combination of Lorentzian and Gaussian functions. The FWHMs of the vignetting curves at $E = 50$ keV are estimated to be 9.9′ and 5.4′ in the θ_Y and θ_Z directions, respectively. Since the FWHM in the θ_Z direction is smaller than that of θ_Y, the vignetting curve has "insensitive" and "sensitive" directions. The FWHM at $E = 50$ keV is smaller than that at $E = 30$ keV, because x rays in a higher energy band are reflected at an inner radius.

We deduced the optical axis of HXT from the peak positions of the vignetting curves. Figure 21 shows the peak position of each segment on the θ_Y–θ_Z plane. The origin of this plane indicates the designed position of the optical axis of HXT. To deduce the

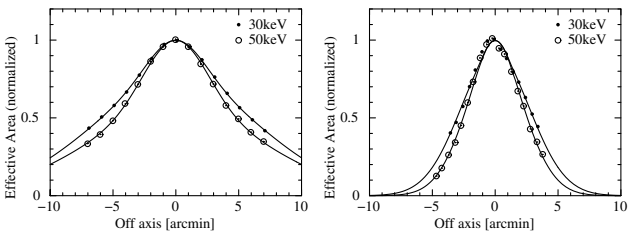

Fig. 20. Vignetting curves of segment 1 of HXT-1 in the θ_Y (left) and θ_Z (right) directions. Filled and open circles display the data at $E = 30$ and 50 keV, respectively. The data were fitted with a combination of Lorentzian and Gaussian functions. The solid lines indicate the best fit models.

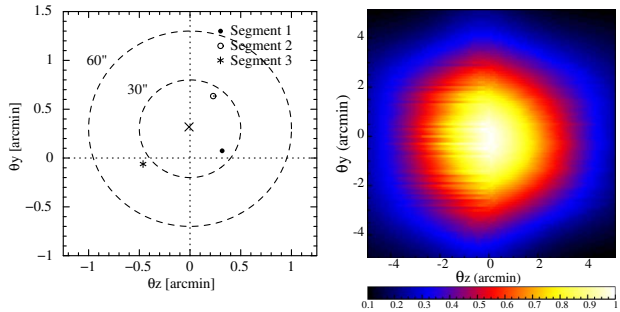

Fig. 21. Optical axes of HXT-1 measured at SPring-8 (left) and summed vignetting function of HXT-1 (right). The left figure displays the optical axis of each segment deduced from the vignetting curve. The cross indicates the optical axis of HXT-1.

vignetting function of the full telescope, we assumed the vignetting function $f_{\mathrm{i}}(\theta_Y, \theta_Z)$ of the ith segment as

$$f_{\mathrm{i}}(\theta_Y, \theta_Z) = (\text{Lorentzian} + \text{Gaussian})_{\text{sensitive}} \times (\text{Lorentzian} + \text{Gaussian})_{\text{insensitive}}.$$

Summing the vignetting function of each segment, we obtained the vignetting function of a full telescope (see Fig. 21). The summed vignetting function has a maximum value at $(\theta_Y^{\mathrm{MAX}}, \theta_Z^{\mathrm{MAX}}) = (0.0', 0.3')$. We plot $(\theta_Y^{\mathrm{MAX}}, \theta_Y^{\mathrm{MAX}})$ in Fig. 21, and we redefine $(\theta_Y^{\mathrm{MAX}}, \theta_Z^{\mathrm{MAX}})$ as the direction of the optical axis of HXT-1. The HXT FOV at 50 keV is estimated to be 5.6′.

5. Conclusion

ASTRO-H will carry two HXTs, which are called HXT-1 and HXT-2. We have designed HXTs to achieve the performance required for the scientific objectives of this project under the given boundary conditions. The mirror production of HXTs was completed by March 2012 for HXT-1 and by March 2013 for HXT-2. In the fabrication, we produced more than 4000 reflectors for HXTs, and selected 2556 reflectors for the flight hardware. After the integration of HXTs, we carried out ground calibrations at the synchrotron radiation facility, SPring-8. It was found that two HXTs have quite similar x-ray performance. The HPD and effective area are ~1.9′ and ~175 cm^2 at 30 keV, which are close to the requirements for HXT.

Since HXT will cover the energy region below 10 keV as well as the hard x-ray region, we started the calibration of HXT below 10 keV at ISAS/JAXA in September 2014. The calibration will be finished by the end of 2014. After the calibration, we will make response functions by using the ray-tracing simulator. Detailed analysis is in progress for reflecting calibration results on the ray-tracing simulator.

The authors are grateful to all full-time engineers and part-time workers at Nagoya University for support in the mass production of the HXT mirror reflectors. We thank Dr. Hans Krimm (NASA/GSFC) for his comments. We also thank the referee for the valuable comments. The x-ray measurement was

performed at BL20B2 in SPring-8, with the approval of the Japan Synchrotron Radiation Research Institute (JASRI) (Proposal Nos. 2009A0088, 2009B0088, 2010A0088, 2010B0088, 2011A0088, 2011B0088, 2012A0088, 2012B0088, 2013A0088, and 2013B0088).

References

1. W. Voges, B. Aschenbach, T. Boller, H. Bräuninger, U. Briel, W. Burkert, K. Dennerl, J. Englhauser, R. Gruber, F. Haberl, G. Hartner, G. Hasinger, M. Kürster, E. Pfeffermann, W. Pietsch, P. Predehl, C. Rosso, J. H. M. M. Schmitt, J. Trümper, and H. U. Zimmermann, "The ROSAT all-sky survey bright source catalogue," Astron. Astrophys. **349**, 389–405 (1999).
2. Y. Tanaka, H. Inoue, and S. S. Holt, "The astronomy satellite ASCA," Publ. Astron. Soc. Jpn. **46**, L37–L41 (1994).
3. P. J. Serlemitsos, L. Jalota, Y. Soong, H. Kunieda, Y. Tawara, Y. Tsusaka, H. Suzuki, Y. Sakima, T. Yamazaki, H. Yoshioka, A. Furuzawa, K. Yamashita, H. Awaki, M. Itoh, Y. Ogasaka, H. Honda, and Y. Uchibori, "The X-ray telescope on board ASCA," Publ. Astron. Soc. Jpn. **47**, 105–114 (1995).
4. P. J. Serlemitsos, Y. Soong, K.-W. Chan, T. Okajima, J. P. Lehan, Y. Maeda, K. Itoh, H. Mori, R. Iizuka, A. Itoh, H. Inoue, S. Okada, Y. Yokoyama, Y. Itoh, M. Ebara, R. Nakamura, K. Suzuki, M. Ishida, A. Hayakawa, C. Inoue, S. Okuma, R. Kubota, M. Suzuki, T. Osawa, K. Yamashita, H. Kunieda, Y. Tawara, Y. Ogasaka, A. Furuzawa, K. Tamura, R. Shibata, Y. Haba, M. Naitou, and K. Misaki, "The X-ray telescope onboard Suzaku," Publ. Astron. Soc. Jpn. **59**, S9–S21 (2007).
5. K. Yamashita, P. J. Serlemitsos, J. Tueller, S. D. Barthelmy, L. M. Bartlett, K.-W. Chan, A. Furuzawa, N. Gehrels, K. Haga, H. Kunieda, P. Kurczynski, G. Lodha, N. Nakajo, N. Nakamura, and Y. Namba, "Supermirror hard-x-ray telescope," Appl. Opt. **37**, 8067–8073 (1998).
6. T. Okajima, K. Tamura, Y. Ogasaka, K. Haga, S. Takahashi, S. Ichimaru, H. Kito, S. Fukuda, A. Goto, and K. Nomoto, "Characterization of the supermirror hard-x-ray telescope for the InFOCμS balloon experiment," Appl. Opt. **41**, 5417–5426 (2002).
7. F. Berendse, S. M. Owens, P. J. Serlemitsos, J. Tueller, K.-W. Chan, Y. Soong, H. Krimm, W. H. Baumgartner, Y. Ogasaka, K. Tamura, T. Okajima, Y. Tawara, K. Yamashita, K. Misaki, and H. Kunieda, "Production and performance of the InFOCμS 20–40 keV graded multilayer mirror," Appl. Opt. **42**, 1856–1866 (2003).
8. Y. Ogasaka, J. Tueller, K. Yamashita, P. J. Serlemitsos, R. Shibata, K. Tamura, A. Furuzawa, T. Miyazawa, R. Takahashi, M. Sakashita, K. Shimoda, Y. Tawara, H. Kunieda, T. Okajima, H. Krimm, S. Barthelmy, Y. Soong, K.-W. Chan, S. Owens, M. Rex, E. Chapin, and M. Devlin, "First light of a hard-x-ray imaging experiment: the InFOCμS balloon flight," Proc. SPIE **5900**, 217–224 (2005).
9. F. A. Harrison, W. W. Craig, F. E. Christensen, C. J. Hailey, W. W. Zhang, S. E. Boggs, D. Stern, W. R. Cook, K. Forster, P. Giommi, B. W. Grefenstette, Y. Kim, T. Kitaguchi, J. E. Koglin, K. K. Madsen, P. H. Mao, H. Miyasaka, K. Mori, M. Perri, M. J. Pivovaroff, S. Puccetti, V. R. Rana, N. J. Westergaard, J. Willis, A. Zoglauer, H. An, M. Bachetti, N. M. Barrière, E. C. Bellm, V. Bhalerao, N. F. Brejnholt, F. Fuerst, C. C. Liebe, C. B. Markwardt, M. Nynka, J. K. Vogel, D. J. Walton, D. R. Wik, D. M. Alexander, L. R. Cominsky, A. E. Hornschemeier, A. Hornstrup, V. M. Kaspi, G. M. Madejski, G. Matt, S. Molendi, D. M. Smith, J. A. Tomsick, M. Ajello, D. R. Ballantyne, M. Baloković, D. Barret, F. E. Bauer, R. D. Blandford, W. N. Brandt, L. W. Brenneman, J. Chiang, D. Chakrabarty, J. Chenevez, A. Comastri, F. Dufour, M. Elvis, A. C. Fabian, D. Farrah, C. L. Fryer, E. V. Gotthelf, J. E. Grindlay, D. J. Helfand, R. Krivonos, D. L. Meier, J. M. Miller, L. Natalucci, P. Ogle, E. O. Ofek, A. Ptak, S. P. Reynolds, J. R. Rigby, G. Tagliaferri, S. E. Thorsett, E. Treister, and C. M. Urry, "The nuclear spectroscopic telescope array (NuSTAR) high-energy x-ray mission," Astrophys. J. **770**, 103 (2013).
10. T. Takahashi, K. Mitsuda, R. Kelley, F. Aharonian, F. Akimoto, S. Allen, N. Anabuki, L. Angelini, K. Arnaud, H. Awaki, A. Bamba, N. Bando, M. Bautz, R. Blandford, K. Boyce, G. Brown, M. Chernyakova, P. Coppi, E. Costantini, J. Cottam, J. Crow, J. J. de Plaa, C. de Vries, J.-W. den Herder, M. Dipirro, C. Done, T. Dotani, K. Ebisawa, T. Enoto, Y. Ezoe, A. Fabian, R. Fujimoto, Y. Fukazawa, S. Funk, A. Furuzawa, M. Galeazzi, P. Gandhi, K. Gendreau, K. Gilmore, Y. Haba, K. Hamaguchi, I. Hatsukade, K. Hayashida, J. Hiraga, K. Hirose, A. Hornschemeier, J. Hughes, U. Hwang, R. Iizuka, K. Ishibashi, M. Ishida, K. Ishimura, Y. Ishisaki, N. Isobe, M. Ito, N. Iwata, J. Kaastra, T. Kallman, T. Kamae, H. Katagiri, J. Kataoka, S. Katsuda, M. Kawaharada, N. Kawai, S. Kawasaki, D. Khangaluyan, C. Kilbourne, K. Kinugasa, S. Kitamoto, T. Kitayama, T. Kohmura, M. Kokubun, T. Kosaka, T. Kotani, K. Koyama, A. Kubota, H. Kunieda, P. Laurent, F. Lebrun, O. Limousin, M. Loewenstein, K. Long, G. Madejski, Y. Maeda, K. Makishima, M. Markevitch, H. Matsumoto, K. Matsushita, D. McCammon, J. Miller, S. Mineshige, K. Minesugi, T. Miyazawa, T. Mizuno, K. Mori, H. Mori, K. Mukai, H. Murakami, T. Murakami, R. Mushotzky, Y. Nakagawa, T. Nakagawa, H. Nakajima, T. Nakamori, K. Nakazawa, Y. Namba, M. Nomachi, S. O'Dell, H. Ogawa, M. Ogawa, K. Ogi, T. Ohashi, M. Ohno, M. Ohta, T. Okajima, N. Ota, M. Ozaki, F. Paerels, S. Paltani, A. Parmar, R. Petre, M. Pohl, S. Porter, B. Ramsey, C. Reynolds, S. Sakai, R. Sambruna, G. Sato, Y. Sato, P. Serlemitsos, M. Shida, T. Shimada, K. Shinozaki, P. Shirron, R. Smith, G. Sneiderman, Y. Soong, L. Stawarz, H. Sugita, A. Szymkowiak, H. Tajima, H. Takahashi, Y. Takei, T. Tamagawa, T. Tamura, K. Tamura, T. Tanaka, Y. Tanaka, Y. Tanaka, M. Tashiro, Y. Tawara, Y. Terada, Y. Terashima, F. Tombesi, H. Tomida, M. Tozuka, Y. Tsuboi, M. Tsujimoto, H. Tsunemi, T. Tsuru, H. Uchida, Y. Uchiyama, H. Uchiyama, Y. Ueda, S. Uno, M. Urry, S. Watanabe, N. White, T. Yamada, H. Yamaguchi, K. Yamaoka, N. Yamasaki, M. Yamauchi, S. Yamauchi, Y. Yatsu, D. Yonetoku, and A. Yoshida, "ASTRO-H mission," Proc. SPIE **7732**, 77320Z (2010).
11. Y. Ogasaka, K. Tamura, T. Miyazawa, Y. Fukaya, T. Iwahara, N. Sasaki, A. Furuzawa, Y. Haba, Y. Kanou, D. Ueno, H. Kunieda, K. Yamashita, R. Shibata, T. Okajima, J. Tueller, P. Serlemitsos, Y. Soong, K.-W. Chan, E. Miyata, H. Tsunemi, K. Uesugi, Y. Suzuki, and Y. Namba, "Thin-foil multilayer-supermirror hard X-ray telescopes for InFOCμS/SUMIT balloon experiments and NeXT satellite program," Proc. SPIE **6688**, 668803 (2007).
12. K. Ito, K. Ogi, H. Awaki, T. Koasaka, and Y. Yamamoto, "The thermal analysis of the hard X-ray telescope (HXT) and the investigation of the deformation of the mirror foil due to temperature change," Proc. SPIE **8147**, 814704 (2011).
13. H. Kunieda, H. Awaki, A. Furuzawa, Y. Haba, R. Iizuka, K. Ishibashi, M. Ishida, M. Itoh, T. Kosaka, Y. Maeda, H. Matsumoto, T. Miyazawa, H. Mori, Y. Namba, Y. Ogasaka, K. Ogi, T. Okajima, Y. Suzuki, K. Tamura, Y. Tawara, K. Uesugi, K. Yamashita, and S. Yamauchi, "Hard X-ray telescope to be onboard ASTRO-H," Proc. SPIE **7732**, 773214 (2010).
14. Y. Miyata, K. Tamura, and H. Kunieda, "New multilayer design for ASTRO-H/hard X-ray telescope and missions beyond," Proc. SPIE **8147**, 81470V (2011).
15. S. Sasaki, "Numerical tables of anomalous scattering factors calculated by the Cromer and Liberman's method," KEK Report 88-14, 1989.
16. S. Sasaki, "X-ray absorption coefficients of the elements (Li to Bi, U)," KEK Report 90-16, 1990.
17. H. Mori, R. Iizuka, R. Shibata, Y. Haba, A. Hayakawa, A. Hayashi, C. Inoue, H. Inoue, M. Ishida, A. Itoh, K. Itoh, H. Kunieda, Y. Maeda, K. Misaki, M. Naitou, S. Okada, T. Shimizu, and Y. Yokoyama, "Pre-collimator of the Astro-E2 X-ray telescopes for stray-light reduction," Publ. Astron. Soc. Jpn. **57**, 245–257 (2005).
18. H. Mori, Y. Ogasaka, M. Ishida, Y. Maeda, K. Tamura, H. Kunieda, A. Furuzawa, Y. Haba, T. Miyazawa, K. Yamashita, H. Awaki, P. J. Serlemitsos, Y. Soong, K.-W. Chan, and

T. Okajima, "Design of the pre-collimator for the NeXT X-ray telescopes," Proc. SPIE **7011**, 70112W (2008).
19. H. Mori, Y. Haba, T. Miyazawa, A. Furuzawa, Y. Tawara, H. Kunieda, S. Yamauchi, H. Awaki, M. Ishida, Y. Maeda, A. Bamba, R. Iizuka, T. Okajima, and R. Mushotzky, "Current status of the pre-collimator development for the ASTRO-H X-ray telescopes," Proc. SPIE **7732**, 77323E (2010).
20. Y. Tawara, S. Sugita, A. Furuzawa, K. Tachibana, H. Awaki, M. Ishida, Y. Maeda, and M. Ogawa, "Development of ultra-thin thermal shield for ASTRO-H X-ray telescopes," Proc. SPIE **8147**, 814704 (2011).
21. B. L. Henke, E. M. Gullikson, and J. C. Davis, "X-ray interactions: photoabsorption, scattering, transmission, and reflection at E = 50–30000 eV, Z = 1–92," At. Data Nucl. Data Tables **54**, 181–342 (1993).
22. A. Furuzawa, Y. Ogasaka, H. Kunieda, T. Miyazawa, M. Sakai, Y. Kinoshita, Y. Makinae, S. Sasaya, Y. Kanou, D. Niki, T. Ohgi, N. Oishi, K. Yamane, N. Yamane, Y. Ishida, Y. Haba, Y. Tawara, K. Yamashita, M. Ishida, Y. Maeda, H. Mori, K. Tamura, H. Awaki, and T. Okajima, "The current status of ASTRO-H/HXT development facility," Proc. SPIE **7437**, 743709 (2009).
23. H. Awaki, H. Kunieda, A. Furuzawa, Y. Haba, T. Hayashi, R. Iizuka, K. Ishibashi, M. Ishida, M. Itoh, T. Kosaka, Y. Maeda, H. Matsumoto, T. Miyazawa, H. Mori, H. Nagano, Y. Namba, Y. Ogasaka, K. Ogi, T. Okajima, S. Sugita, Y. Suzuki, K. Tamura, Y. Tawara, K. Uesugi, K. Yamashita, and S. Yamauchi, "Current status of ASTRO-H hard x-ray telescopes (HXTs)," Proc. SPIE **8443**, 844324 (2012).
24. S. Goto, K. Takeshita, Y. Suzuki, H. Ohashi, Y. Asano, H. Kimura, T. Matsushita, N. Yagi, M. Isshiki, H. Yamazaki, Y. Yoneda, K. Umetani, and T. Ishikawa, "Construction and commissioning of a 215-m-long beamline at SPring-8," Nucl. Instrum. Methods Phys. Res. Sect. A **467**, 682–685 (2001).
25. Y. Ogasaka, K. Tamura, R. Shibata, A. Furuzawa, T. Miyazawa, K. Shimoda, Y. Fukaya, T. Iwahara, T. Nakamura, M. Naitou, Y. Kanou, N. Sasaki, D. Ueno, T. Okajima, E. Miyata, N. Tawa, K. Mukai, K. Ikegami, M. Aono, K. Uesugi, Y. Suzuki, S. Takeuchi, T. Futamura, R. Takahashi, M. Sakashita, C. Sakai, M. Nonoyama, N. Yamada, K. Onishi, T. Miyauchi, Y. Maeda, S. Okada, P. Serlemitsos, Y. Soong, K.-W. Chan, S. Rohrbach, F. Berendse, J. Tueller, H. Tsunemi, H. Kunieda, and K. Yamashita, "Characterization of a hard X-ray telescope at synchrotron facility SPring-8," Jpn. J. Appl. Phys. **47**, 5743–5754 (2008).
26. T. Miyazawa, Y. Ogasaka, T. Iwahara, Y. Kanou, N. Sasaki, Y. Makinae, S. Sasaya, Y. Inukai, A. Furuzawa, Y. Haba, H. Kunieda, K. Yamashita, K. Uesugi, Y. Suzuki, K. Tamura, Y. Maeda, M. Ishida, and T. Okajima, "Hard X-ray characterization of the NeXT hard X-ray telescopes at SPring-8," Proc. SPIE **7011**, 70112P (2008).
27. T. Miyazawa, A. Furuzawa, Y. Kanou, K. Matsuda, M. Sakai, N. Yamane, Y. Ishida, S. Hara, Y. Miyata, K. Sakanobe, Y. Haba, H. Matsumoto, Y. Tawara, H. Kunieda, H. Mori, K. Tamura, Y. Maeda, M. Ishida, H. Awaki, T. Okajima, K. Uesugi, Y. Suzuki, N. Ishida, N. Ohtsu, A. Suzuki, Y. Ogasaka, and K. Yamashita, "Current status of hard X-ray characterization of ASTRO-H HXT at SPring-8," Proc. SPIE **7732**, 77323 (2010).
28. D. Spiga, "Analytical evaluation of the X-ray scattering contribution to imaging degradation in grazing-incidence X-ray telescopes," Astron. Astrophys. **468**, 775–784 (2007).